

Article

# Modeling Temperature-Dependent Thermoelectric Performance of Magnesium-Based Compounds for Energy Conversion Efficiency Enhancement Using Intelligent Computational Methods

Sami M. Ibn Shamsah 

Department of Mechanical Engineering, College of Engineering, University of Hafr Al Batin, P.O. Box 1803, Hafr Al Batin 31991, Saudi Arabia; sibnshamsah@uhb.edu.sa

**Abstract:** Eco-friendly magnesium-based thermoelectric materials have recently attracted significant attention in green refrigeration technology and wasted heat recovery applications due to their cost effectiveness, non-toxicity, and earth abundance. The energy conversion efficiency of these thermoelectric materials is controlled by a dimensionless thermoelectric figure of merit (TFM), which depends on thermal and electrical conductivity. The independent tuning of the electrical and thermal properties of these materials for TFM enhancement is challenging. The improvement in the TFM of magnesium thermoelectric materials through scattering and structural engineering is experimentally challenging, especially if multiple elements are to be incorporated at different concentrations and at different doping sites. This work models the TFM of magnesium-based thermoelectric materials with the aid of single-hidden-layer extreme learning machine (ELM) and hybrid genetic-algorithm-based support vector regression (GSVR) algorithms using operating absolute temperature, elemental ionic radii, and elemental concentration as descriptors. The developed TFM-G-GSVR model (with a Gaussian mapping function) outperforms the TFM-S-ELM model (with a sine activation function) using magnesium-based thermoelectric testing samples with improvements of 17.06%, 72%, and 73.03% based on correlation coefficient (CC), root mean square error (RMSE), and mean absolute error (MAE) assessment metrics, respectively. The developed TFM-P-GSVR (with a polynomial mapping function) also outperforms TFM-S-ELM during the testing stage, with improvements of 14.59%, 55.31%, and 62.86% using CC, RMSE, and MAE assessment metrics, respectively. Also, the developed TFM-G-ELM model (with a sigmoid activation function) shows superiority over the TFM-S-ELM model with improvements of 14.69%, 79.52%, and 83.82% for CC, RMSE, and MAE assessment yardsticks, respectively. The dependence of some selected magnesium-based thermoelectric materials on temperature and dopant concentration on TFM was investigated using the developed model, and the predicted patterns align excellently with the reported values. This unique performance demonstrated that the developed intelligent models can strengthen room-temperature magnesium-based thermoelectric materials for industrial and technological applications in addressing the global energy crisis.

**Keywords:** thermoelectric figure of merit; extreme learning machine; ionic radii; genetic algorithm; magnesium-based materials; support vector regression



**Citation:** Ibn Shamsah, S.M. Modeling Temperature-Dependent Thermoelectric Performance of Magnesium-Based Compounds for Energy Conversion Efficiency Enhancement Using Intelligent Computational Methods. *Inorganics* **2024**, *12*, 85. <https://doi.org/10.3390/inorganics12030085>

Academic Editors: Torben R. Jensen, Paolo Mele and Giovanna Latronico

Received: 5 January 2024

Revised: 11 February 2024

Accepted: 4 March 2024

Published: 9 March 2024



**Copyright:** © 2024 by the author. Licensee MDPI, Basel, Switzerland. This article is an open access article distributed under the terms and conditions of the Creative Commons Attribution (CC BY) license (<https://creativecommons.org/licenses/by/4.0/>).

## 1. Introduction

Thermoelectric-based technology has inherent and promising potential to resolve the present environmental issues and energy crisis since it converts wasted heat energy into electricity, and vice versa [1–3]. This technology offers sustainable and clean solutions for the energy crisis, with the application domain cutting across solid-state refrigeration and the harvesting of wasted heat [4]. A dimensionless parameter known as the thermoelectric figure of merit controls the energy conversion efficiency of thermoelectric materials [5].

The need for highly efficient thermoelectric materials is crucial for most applications. This efficiency-measuring parameter is material-dependent and is related to other material properties such as electrical conductivity, the Seebeck coefficient, absolute temperature, and thermal conductivity [6,7]. To strengthen thermoelectric properties for improved efficiency, the independent tuning of thermal and electrical conductivity is challenging due to the strong coupling between them from a carrier concentration perspective [8]. Two main approaches adopted recently for energy conversion efficiency improvement include electrical power factor enhancement (through band engineering and carrier concentration optimization) and lattice thermal conductivity reduction via boundary or alloy scattering [8]. Carrier concentration optimization through doping has also been reported to strengthen the thermoelectric figure of merit. The enhancement of thermoelectric properties beyond the optimization of the carrier concentration requires more advanced concepts such as scattering engineering (which includes modulation doping and energy filtering effects) and structural engineering (which includes band convergence, band flattening, a band position that is temperature-dependent, and resonant level) [9]. Recent progress in magnesium-based thermoelectric materials has been reported in the literature [10]. The impact of structure and compositions in enhancing the performance of these compounds in various application domains has been extensively discussed [11,12]. Band convergence that allows the convergence of different bands through temperature change or alloying possibly translates into an increase in the effective mass density of states without carrier mobility being degraded, with the ultimate enhancement of the thermoelectric material's power factor. Intelligent approaches are proposed in this work for modeling and designing magnesium-based thermoelectric materials with the desired energy conversion efficiency. The reason for the selection of the thermoelectric figure of merit is due to the fact that this parameter aggregately controls the energy conversion efficiency of thermoelectric materials.

Magnesium-based thermoelectric materials have the characteristic of an excellent and tunable thermoelectric figure of merit attributed to the presence of a multivalley conduction band close to the Fermi level, which creates room for performance optimization [13,14]. Another significant factor governing the choice of thermoelectric materials for technology applications is the cost of the synthesis materials [15]. The commercially available thermoelectric materials such as tellurium-based compounds are costly and extremely scarce, which limits industrial production [8]. The approaches used for identifying and preparing thermoelectric materials with a high figure of merit include the introduction of extrinsic features into existing thermoelectric materials and searching for pristine materials with intrinsic mechanisms of transportation [16]. Efforts are ongoing for the exploration of low-cost thermoelectric materials with the characteristic of high energy conversion efficiency. As such, magnesium-based materials are promising candidates due to their inexpensive constituent elements, non-toxicity, and abundance [17]. Additionally, the excess magnesium in the prepared magnesium-based thermoelectric samples forms an integral part of the interstitials, resulting in improved performance [4,16]. Magnesium-based thermoelectric materials such as magnesium stannides have further attracted significant attention due to the ease of tuning their thermoelectric figure of merit and their adjustable power factor [18]. The power factor is the product of the square of the Seebeck coefficient and electrical conductivity. Enhancement of the thermoelectric figure of merit demands an increase in power factor and a reduction in lattice thermal conductivity. The single parabolic band framework captures the power-factor-tuning mechanism of most magnesium-based thermoelectric materials [8]. The energy conversion efficiency of magnesium-based thermoelectric materials is influenced by band convergence, point defects and scattering potentials [15]. However, thermal conductivity due to lattice is relatively high in magnesium-based thermoelectric materials as compared to other thermoelectric materials. Reduction in lattice thermal conductivity through dopant incorporation translates to enhance thermoelectric figure of merit (TFM). Challenges of independently tuning the thermal and electrical conductivity of magnesium-based thermoelectric materials for improved energy conversion efficiency coupled with laborious experimental procedures is of serious concern which calls for the

need for theoretical and computational modeling approaches. This work employs empirical (extreme learning machine algorithm) and structural support vector regression algorithm) risk minimization principle based intelligent algorithms to model the energy conversion efficiency of magnesium-based thermoelectric materials using temperature, elemental ionic radii and elemental concentration descriptors.

Support vector regression (SVR) is a powerful intelligent learning algorithm employed in addressing regression tasks [19,20]. It is an extension of support vector machines and operates by finding a hyper-plane in a high-dimensional space that best represents the relationship between input variables and the corresponding output [21]. SVR excels in capturing complex patterns and non-linear relationships in data samples, making it particularly suitable for tasks where traditional linear regression models may fall short. Since limited samples characterize magnesium-based thermoelectric materials, the choice of SVR algorithm for modeling is perfect since the algorithm has been reported to perform excellently well when developed using few data samples [22–24]. For effective modeling of TFM of magnesium-based thermoelectric materials using the SVR intelligent algorithm, optimization of SVR parameters was conducted using a genetic meta-heuristic algorithm. Genetic algorithm (GA) is an optimization technique inspired by the principles of natural selection and genetics [25]. It belongs to the family of evolutionary algorithms and is employed to find optimal solutions to complex problems. Mimicking the process of natural selection, GA iteratively evolves a population of potential solutions through the application of genetic operators such as mutation, crossover, and selection [26]. Widely used in various fields, GA proves especially effective in solving problems with multiple variables and intricate solution spaces [27–29]. The unique features of genetically optimized support vector regression (GSVR) are harnessed in this present work to model energy conversion efficiency of magnesium-based thermoelectric materials.

Extreme learning machine (ELM) intelligent algorithm slightly departs from the conventional neural network training methods in terms of its weight initialization scheme [30,31]. Model training in ELM involves random weight assignment in the input-hidden layer connections. This approach expedites training speed and enhances generalization capabilities, thus allowing it effectively adapt to diverse and high-dimensional data samples [32,33]. The energy conversion efficiency of magnesium-based thermoelectric materials is also modeled using a single hidden layer extreme learning machine intelligence algorithm with sine and sigmoid activation functions.

The outcomes of the modeling and simulation show that the developed TFM-S-ELM model (with sine activation function) performs better than TFM-G-GSVR (with Gaussian mapping function), TFM-P-GSVR (with polynomial mapping function) and TFM-G-ELM (with sigmoid activation function) models with improvements of 1.70%, 27.96% and 64.52% using correlation coefficient (CC) on training magnesium thermoelectric samples. Additionally, the TFM-G-GSVR model outperforms the TFM-S-ELM model during the testing phase with improvements of 17.06%, 72% and 73.03% using CC, root mean square error (RMSE) and mean absolute error (MAE) assessment metrics, respectively. The developed TFM-P-GSVR also outperforms TFM-S-ELM with improvements of 14.59%, 55.31% and 62.86% using CC, RMSE and MAE assessment metrics, respectively. Also, the developed TFM-G-ELM model shows superiority over the TFM-S-ELM model with improvements of 14.69%, 79.52% and 83.82%, for CC, RMSE and MAE assessment yardsticks, respectively.

The organization and outline of the rest of the manuscript are as follows: Section 2 mathematically formulates the employed intelligent and optimization algorithms which include support vector regression, extreme learning machine and genetic algorithm. Section 3 describes the modified chemical formula of magnesium-based thermoelectric materials with four different elemental inclusions. The detailed computational description of the intelligent algorithms is also contained in Section 3. Section 4 presents the modeling results, convergence patterns of the optimization algorithm and performance comparison using different assessment parameters. The influences of temperature and dopants on

magnesium-based thermoelectric materials are also presented in Section 4. The conclusions drawn from the research work are presented in Section 5 of the manuscript.

## 2. Mathematical Formulation and Background of the Implemented Algorithms

Formulations of the implemented algorithms are described mathematically in this section. The described mathematical formulations include support vector regression, extreme learning machine and genetic meta-heuristic optimization evolutionary algorithm.

### 2.1. Support Vector Regression Description

Support vector regression (SVR) effectively addresses and characterizes non-linear systems as a result of the robust underlying structural risk minimization principle inherent to the algorithm [34–36]. Given thermoelectric magnesium-based materials  $(\beta_k, \tau_k^*)^n$ ,  $\beta_k$  represents the input descriptive vectors, which include the operating temperature, ionic radii of the elemental compositions as well as the elemental concentrations, while  $\tau$  denotes the corresponding measured thermoelectric figure of merit. The algorithm employs the regression function outlined in Equation (1) to model the system [37].

$$\tau(\beta) = \langle w, \beta \rangle + \phi \quad (1)$$

Here,  $\tau$  signifies the predicted thermoelectric figure of merit obtained through the SVR algorithm. The undetermined coefficients  $w$  and  $\phi$  representing the weight vector and bias are deduced by minimizing the risk function presented in Equation (2) [38].

$$r(\tau) = \frac{v}{m} \sum_{k=1}^n I(\tau(\beta) - \tau_k^*) + \frac{\|\chi\|^2}{2} \quad (2)$$

Here,  $\|\chi\|^2$  denotes the Euclidean norm,  $I$  stands for epsilon insensitive loss function illustrated in Equation (3), and  $v$  represents the penalty factor. The penalty factor imposes a penalty on samples deviating beyond the error epsilon threshold. It is a user-defined constant and non-zero value that can be adjusted through manual tuning or evolutionary algorithms.

$$I(\tau(\beta) - \tau_k^*) = \begin{cases} \|\tau(\beta) - \tau_k^*\| - \epsilon & |\tau(\beta) - \tau_k^*| \geq \epsilon \\ 0 & \tau(\beta) - \tau_k^* < \epsilon \end{cases} \quad (3)$$

It is imperative to incorporate slack variables and  $\tau_k^*$ , particularly in situations where there is a potential risk of surpassing the error threshold. These slack variables govern the separation distance between the measured values and the boundary values. The resultant dual problem is addressed through an optimization approach depicted in Equation (4) [39].

$$\text{Minimize : } \frac{1}{2} \sum_k^n \sum_i^n (\eta_k - \eta_k^*)(\eta_i - \eta_i^*) \lambda(\beta_k, \beta_i) + \sum_{k=1}^n \tau_k^*(\eta_k - \eta_k^*) - \epsilon \sum_{k=1}^n (\eta_k + \eta_k^*) \quad (4)$$

The minimization problem that Equation (4) expresses is subjected to constraints outlined in Equation (5).

$$\sum_{k=1}^n (\eta_k + \eta_k^*) = 0, \eta_k, \eta_k^* \in [0, v] \quad (5)$$

Here,  $\eta_k$  and  $\eta_k^*$  represent the Lagrange multipliers utilized in the solution of the optimization problem. The input vectors corresponding to non-zero coefficients in the optimization solutions are termed support vectors. Employing the aforementioned optimization function, the expression shown in Equation (6) depicts the predictions generated by the SVR algorithm.

$$\tau(\beta) = \sum_{k=1}^n (\eta_k - \eta_k^*) \langle \beta_k, \beta \rangle + \phi \quad (6)$$

The kernel function facilitates the transformation of the original problem into a linear problem in a high-dimensional space. This mapping function is denoted in Equation (7), and the ultimate regression estimation equation of the SVR algorithm is expressed in Equation (8).

$$\lambda(\beta_k, \beta_i) = \varphi(\beta_k)\varphi(\beta_i) \quad (7)$$

$$\tau(\beta) = \sum_{k=1}^n (\eta_k - \eta_k^*)\lambda(\beta_k, \beta_i) + \phi \quad (8)$$

In the context of this task, the employed kernel functions incorporate the Gaussian and polynomial functions which are shown in Equation (9) and Equation (10), respectively.

$$\lambda(\beta_k, \beta) = \exp\left(\frac{|\beta_k - \beta|^2}{d}\right) \quad (9)$$

$$\lambda(\beta_k, \beta) = (\beta_k \cdot \beta + 1)^z \quad (10)$$

where  $d$  and  $z$  are the Gaussian and polynomial kernel parameters, respectively.

## 2.2. Extreme Learning Machine Formulation

The extreme learning machine (ELM) is a unique learning algorithm that was developed by Huang [40]. It is designed specifically for single-hidden layer feed-forward neural networks (SLFNs). Unlike the backpropagation (BP) technique in conventional neural networks, with its attendant shortfalls, the ELM has the ability to avoid the need for numerous iterations and local minima problems [41]. It has, therefore, gained widespread usage in classification and regression tasks owing to its superior generalization capabilities, fast learning speed and unresponsiveness to parameters pre-defined by the user [31,42–46]. The ELM algorithm works by randomly generating the input weights and biases of the hidden layer. Subsequently, it determines the weights of the output layer through analytical methods. Through these techniques, the ELM algorithm achieves better performance in regression tasks. Given a dataset containing  $K$  samples  $(n_i, m_i)$ , where  $n \in R^d$  and  $m \in \Phi$ , the ELM algorithm conveniently models and approximates the linking patterns and functions using the expression shown in Equation (11).

$$\sum_i^J \psi_i \cdot \omega(w_i \cdot n + b_i) = m \quad (11)$$

where  $\omega(x)$  is the activation function,  $w_i$  is the input weight of the  $i$ th node in the hidden layer,  $b_i$  is the corresponding bias,  $\psi_i$  is the output weights, and  $n$ ,  $m$  are the input features and thermoelectric figure of merit, respectively. The model equation above can be expressed more succinctly in matrix form as shown in Equation (12).

$$H\psi = P \quad (12)$$

where  $H$  is the output layer matrix given by

$$H = \begin{pmatrix} h(n_1) \\ \vdots \\ h(n_K) \end{pmatrix} = \begin{pmatrix} \omega(w_1 \cdot n_1 + b_1) & \cdots & \omega(w_J \cdot n_1 + b_J) \\ \vdots & \ddots & \vdots \\ \omega(w_1 \cdot n_K + b_1) & \cdots & \omega(w_J \cdot n_K + b_J) \end{pmatrix}$$

$$\psi = \begin{pmatrix} \psi_1^T \\ \vdots \\ \psi_K^T \end{pmatrix}_{J \times d} \quad \text{and} \quad P = \begin{pmatrix} p_1^T \\ \vdots \\ p_K^T \end{pmatrix}_{K \times d}$$

Output weights  $\psi$  is computed using the smallest norm least square presented in Equation (13) instead of the common optimization method.

$$\psi = H^+P \quad (13)$$

where  $H^+$  is the Moore–Penrose pseudo-inverse of matrix  $H$ . Consequently, this analytical departure from the iterative derivation of the output weights, amongst other things, gave ELM its superior performance over other neuron-based networks.

### 2.3. Genetic Meta-Heuristic Algorithm Principles

Genetic algorithms (GAs) constitute a category of heuristic methods designed for searching optimal solutions and employ the operational principles inspired by biological natural selection [37,47,48]. The algorithm's simplicity, combined with its well-established and robust search mechanisms, has significantly enhanced its applicability in various domains [28,49–52]. The iterative cycles of the genetic algorithm begin with population initialization, wherein a set of potential candidates is introduced into the solution search space. Each of the potential solutions is referred to as an individual within the operational framework of the genetic algorithm [53]. The iteration stages progressively refine the initially created population, adhering to the principle of survival of the fittest, whereby weaker individuals are replaced by more efficient and superior ones. Individuals exhibiting higher fitness are potentially chosen as parents, giving rise to improved offspring for the ensuing iteration. The iterative process continues until the genetic algorithm identifies an individual possessing the optimum solution. Selection, crossover, and mutation constitute the genetic operations; each is assigned a probability value carefully tuned to control the strength and significance of the respective operation.

## 3. Details of the Computation and Model Description

The description of the modified thermoelectric magnesium-based materials is presented in this section with statistical analysis of the employed set of thermoelectric magnesium-based samples. The computational details of both extreme learning machine and hybrid genetic algorithm based support vector regression are described and presented in this section.

### 3.1. Description and Acquisition of Modeling Magnesium-Based Thermoelectric Data Samples

The thermoelectric figure of merit (TFM) for magnesium-based compounds is modeled using intelligent algorithms with ionic radii of elemental constituents, operating temperature and elemental concentration descriptors. The experimental values of thirty different thermoelectric figures of merit for magnesium-based thermoelectric compounds employed for modeling are extracted from the literature [4,6,8,9,13,15,17,54–61]. The modified chemical formula for thermoelectric magnesium-based material is shown in Equation (14).



where  $x$  represents the concentration of magnesium, and where A, B, C and D stand for incorporated elements while  $a$ ,  $b$ ,  $c$  and  $d$  are their respective concentrations. Ten descriptors were employed for each of the developed models. For example, the descriptors for  $\text{Mg}_{1.86}\text{Sn}_{0.837}\text{Si}_{0.093}\text{Na}_{0.14}\text{S}_{0.07}$  magnesium-based compound include the operating temperature of 673, 1.86 (concentration of Mg), ionic radii of Sn, Si, Na and S and their respective concentrations of 0.837, 0.093, 0.14 and 0.07. For a compound with elemental constituents less than four aside, the magnesium, ionic radius and the concentration of the missing element are assigned zero. The choice of the ionic radii descriptors is due to the influence of elemental ionic radii and concentrations in influencing carrier mobility. For instance, low thermal conductivity strengthens the thermoelectric figure of merit while electrons and lattice are partly involved in thermal conductivity. A reduction in thermal conductivity from a phonon contribution perspective can be achieved through phonon scattering center incorporation [62–65]. These centers include nano-inclusions, vacancies, particle size

reduction and elemental substitutions. All these are influenced by the ionic radii and the concentrations of elemental constituents. The statistical analysis results for the dataset are shown in Table 1.

**Table 1.** Analysis of the thermoelectric data samples employed for simulation.

Compound Parameter	Mean	Standard Deviation	Maximum	Minimum	Correlation Coefficient
TFM	1.0397	0.4433	1.8000	0.3600	1.0000
Temperature	679.7333	115.1856	873.0000	423.0000	−0.2122
x	2.2176	0.8213	3.5000	0.9700	0.2235
A	95.2833	24.3047	143.0000	54.0000	0.2522
a	0.4059	0.4531	1.5000	0.0050	−0.0010
B	90.8333	16.7540	117.0000	54.0000	0.3530
b	0.8640	0.6599	2.0000	0.0050	0.2803
C	76.6000	41.0362	117.0000	0.0000	0.4448
c	0.5036	0.7025	2.0000	0.0000	−0.0425
D	14.6000	40.6241	170.0000	0.0000	−0.0624
d	0.0037	0.0133	0.0700	0.0000	−0.1517

Table 1 presents the mean values for all the employed descriptors as well as the measured thermoelectric figure of merit. The standard deviations which measure the consistency in the data samples are also presented in the table. The data sample range can be determined using the presented maximum and minimum values. The coefficient of correlations between each of the predictors and the thermoelectric figure of merit are also contained in Table 1. The operating temperature, the concentration of element A, the concentration of element C, element D and its concentration are negatively correlated with the TFM. The coefficients of correlation for all the predictors are less than 0.5 which indicates a potential weakness in linear function in addressing the relationship. The observed non-linear relationship between the TFM and the presented predictors is well captured in this contribution using non-linear intelligent modeling algorithms which include extreme learning machines and hybrid genetically optimized support vector regression.

### 3.2. Computational Description of Hybrid Intelligent Models

Utilizing the computational environment of MATLAB, the genetic algorithm was integrated with support vector regression for parameter selection, thereby reinforcing the precision domain of the hybridized model. The optimized parameters, including the error epsilon, penalty/regularization factor, and kernel parameter, are determined through the genetic algorithm. Below, the computational details are outlined:

Step 1: In this initial step, the data sample was randomly partitioned into training and testing sets at 8:2 ratio. Prior to partitioning, data randomization was employed to minimize the risk of pattern acquisition from a limited range of samples, thereby reducing the likelihood of under/over-fitting during subsequent model validation.

Step 2: The genetic algorithm begins by defining the search space and initializing the population. Each gene in the genetic algorithm description corresponds to a hyper-parameter targeted for optimization. The specific search space for parameters, including the penalty factor, epsilon, and kernel parameter, was defined as [2000 1, 0.0009 0.0001, 30 15], utilizing the Gaussian mapping function. The upper bounds for the penalty factor, epsilon, and kernel parameter in the search space are set at 2000, 0.0009, and 30, respectively, while the corresponding lower bounds are 1, 0.0001, and 15. This space, however, is specified as [2000 1, 0.0009, 0.0001, 0.008 0.001] for a polynomial mapping function.

Step 3: Here, the fitness was determined by employing the root mean square error (RMSE) of testing thermoelectric magnesium-based samples. The fitness computation involves the following sub-steps: (i) select a kernel function from the array of potential functions iteratively until all is implemented; (ii) integrate the chosen kernel function with a chromosome from the initial population. This produces support vectors that serve as

reproducible models for validation and future use. Chromosome fitness was defined by the RMSE between the experimental and predicted TFM and was calculated for all chromosomes while combining saved support vectors with testing data samples (iii) repeating the initial two steps (i and ii) for other chromosomes and ranking their fitness based on the lowest RMSE values (iv), replicating the entire process for each of all the functions in the kernel function pool. Chromosomes exhibiting superior fitness values are chosen for genetic operations and subsequently passed on to the next generation.

Step 4: The selection operation was implemented at this modeling stage. It involves choosing the best chromosomes based on their fitness function ranking for reproduction and offspring generation. A selection probability of 0.8 was employed, resulting in the production of improved offspring in this modeling stage, which then forms the succeeding population.

Step 5: This step entails the crossover operation which facilitates the transfer of subsequences and portions from parent chromosomes to the new offspring. A crossover probability of 0.9 was implemented to ensure the potential replacement of less fit chromosomes with superior ones in the subsequent iteration.

Step 6: Mutation is carried out in this step. This operation introduces changes by altering random positions within the string. The operation was executed with a probability value of 0.005.

Step 7: A final model is generated if any of the following stopping conditions are met: (i) RMSE value of zero for testing thermoelectric magnesium-based samples; (ii) iteration reaching the maximum number of runs specified at the commencement of simulation; (iii) having the same value of testing RMSE over 50 consecutive iterations. The algorithm flow chart is shown in Figure 1.

### 3.3. Methodology of the Proposed TFM-ELM-Based Models

The computational implementation of the extreme learning machine (ELM) entails the random generation of biases and weights that connect input with a hidden layer within the MATLAB computing environment. Subsequently, the model is trained using 80% of the available thermoelectric magnesium-based data samples, which were randomized to ensure an even distribution. The remaining 20% of the sample was reserved for testing the model's performance. The activation function for the model is chosen from options that include the sine function, the triangular basis, and the sigmoid function. Afterward, the activation function was applied to the hidden layer neurons, and the resulting output matrix was computed. In addition, the weights that connect the hidden layer with the output layer were determined. The schematic description of the ELM implementation procedure is shown in Figure 2 and the source codes for the developed models are contained in the Supplementary Materials.

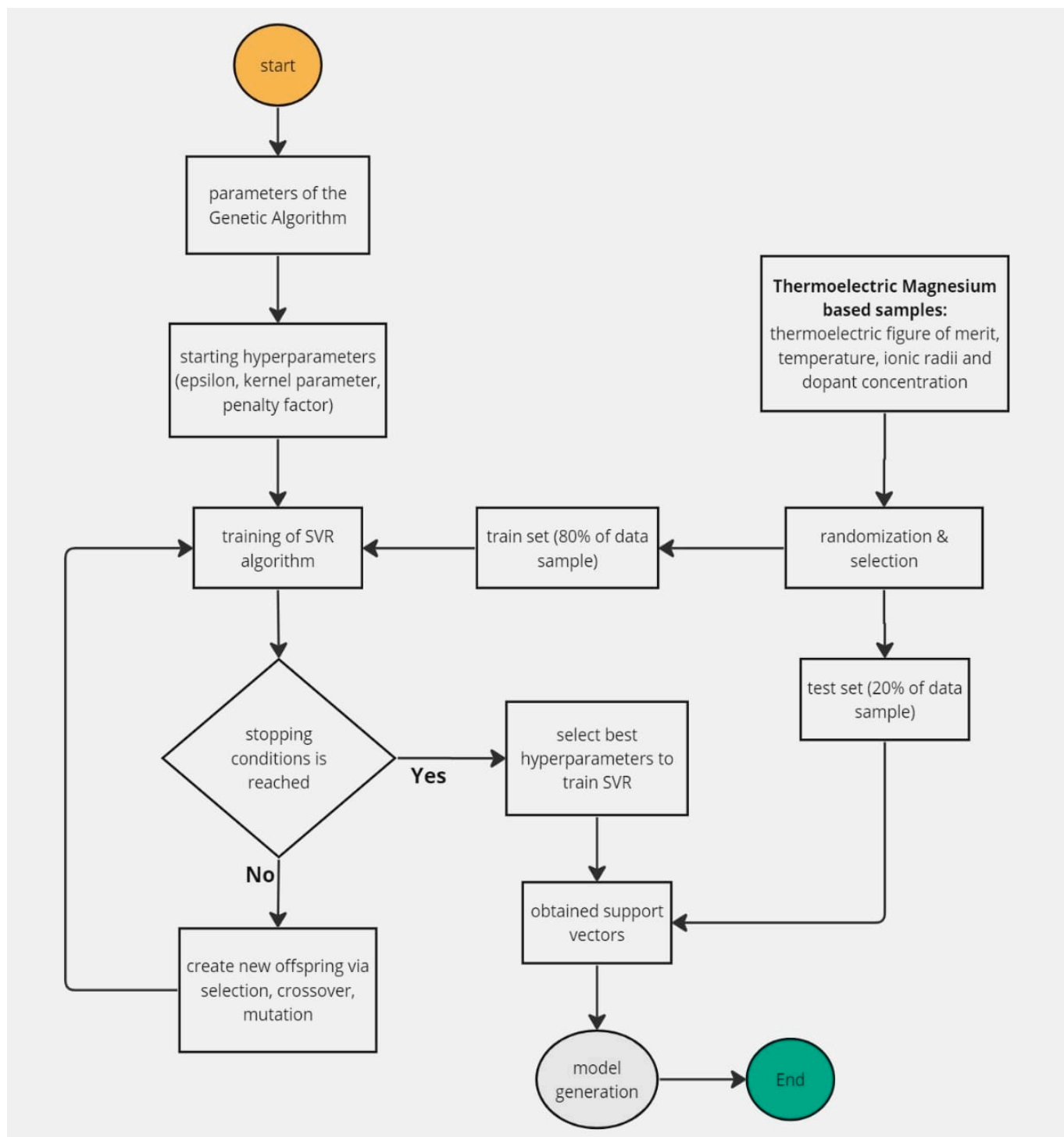


**Figure 1.** Flowchart of the proposed TFM-GSVR-based models.

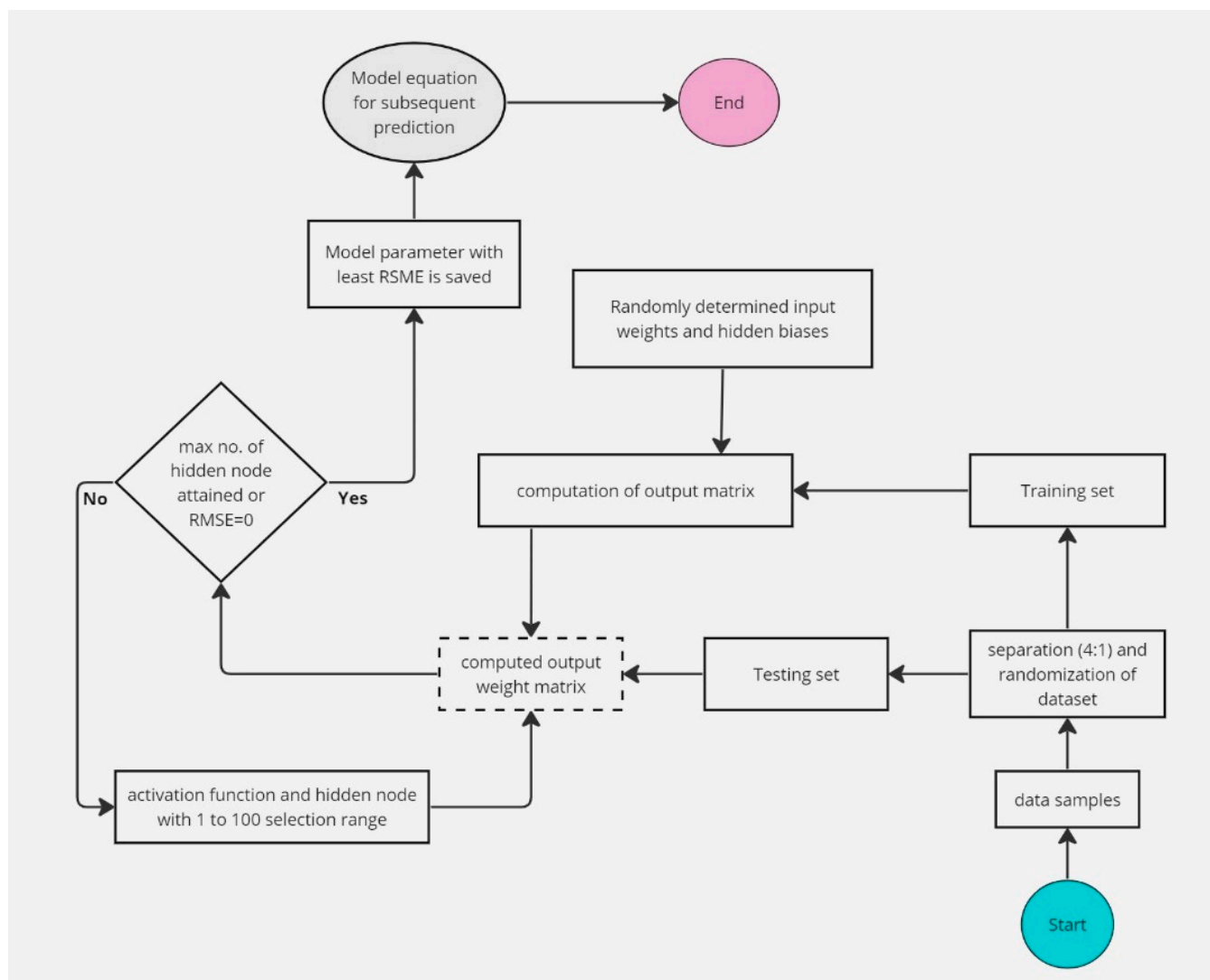


**Figure 2.** Flow chart for the proposed TFM-ELM-based models.

#### 4. Results and Discussion

The outcomes of the thermoelectric figure of merit models developed are discussed in this section together with their performance comparisons. The influence of temperature and dopant concentrations on the thermoelectric figure of merit of selected magnesium-based thermoelectrics is discussed.

##### 4.1. Dependence of Parameter Optimization on Population Size and Iteration Using Genetic Algorithm

Variations in the convergence pattern of the TFM-G-GSVR model at different iterations are presented in Figure 3 for regularization factor (Figure 3a), fitness function (Figure 3b), epsilon error threshold (Figure 3c) and Gaussian mapping parameter (Figure 3d).

Each of the presented parameters converges to global values after ten iterations. The dependence of the number of chromosomes on the exploration and exploitation capacity of the TFM-G-GSVR model is not significantly influenced especially after ten iterations. This is a strong indication that the developed TFM-G-GSVR model is robust and not influenced by population size. For the dependence of the TFM-P-GSVR model on chromosome population size, convergence patterns are depicted in Figure 4. The regularization factor was sought between 2000 and 1 while the genetic optimization algorithm shows the global solution of 1 after 100 iterations as presented in Figure 4a. The fitness function (which is measured

by the root mean square error between the measured thermoelectric figure of merit and the predicted values) is presented in Figure 4b for different chromosome population sizes. One hundred chromosomes could not effectively explore the search space and lead to local convergence as can be observed in Figure 4b.

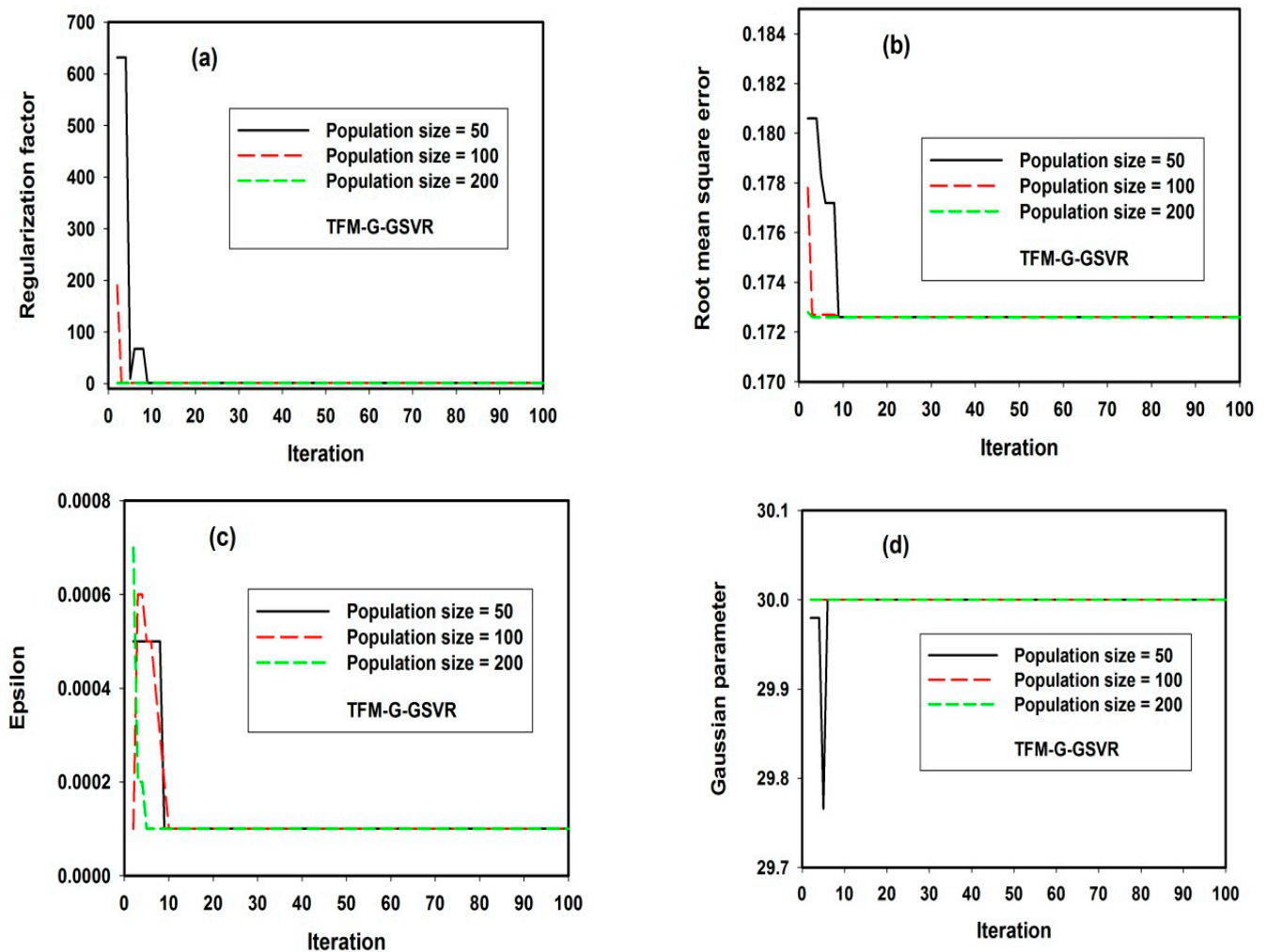


**Figure 3.** Convergence effect of TFM-G-GSVR model on chromosome population size at different iterations: (a) regularization factor; (b) fitness function root mean square error; (c) epsilon error threshold; (d) Gaussian mapping parameter.

A decrease in the number of exploring chromosomes to fifty strengthens the model exploration capacity and with attainment of global convergence. A further increase in participating chromosomes to 200 returns the model convergence to global convergence due to the attainment of balanced exploitation and exploitation strength of the model within search space by a large number of chromosomes. Epsilon error threshold convergence is shown in Figure 4c at three different chromosome sizes (50,100 and 200). The epsilon varied between 0.0009 and 0.0001 during model optimization, and 50 and 200 chromosomes demonstrate similar global convergence patterns. The parameter that controls the ability of polynomial function in data mapping and transformation between feature spaces is shown in Figure 4d for different chromosome population sizes. The population space was sought between 0.008 and 0.001 for optimum convergence. A convergence pattern similar to that of the error threshold was observed. Table 2 shows the optimum values associated with TFM-G-GSVR and TFM-P-GSVR models.

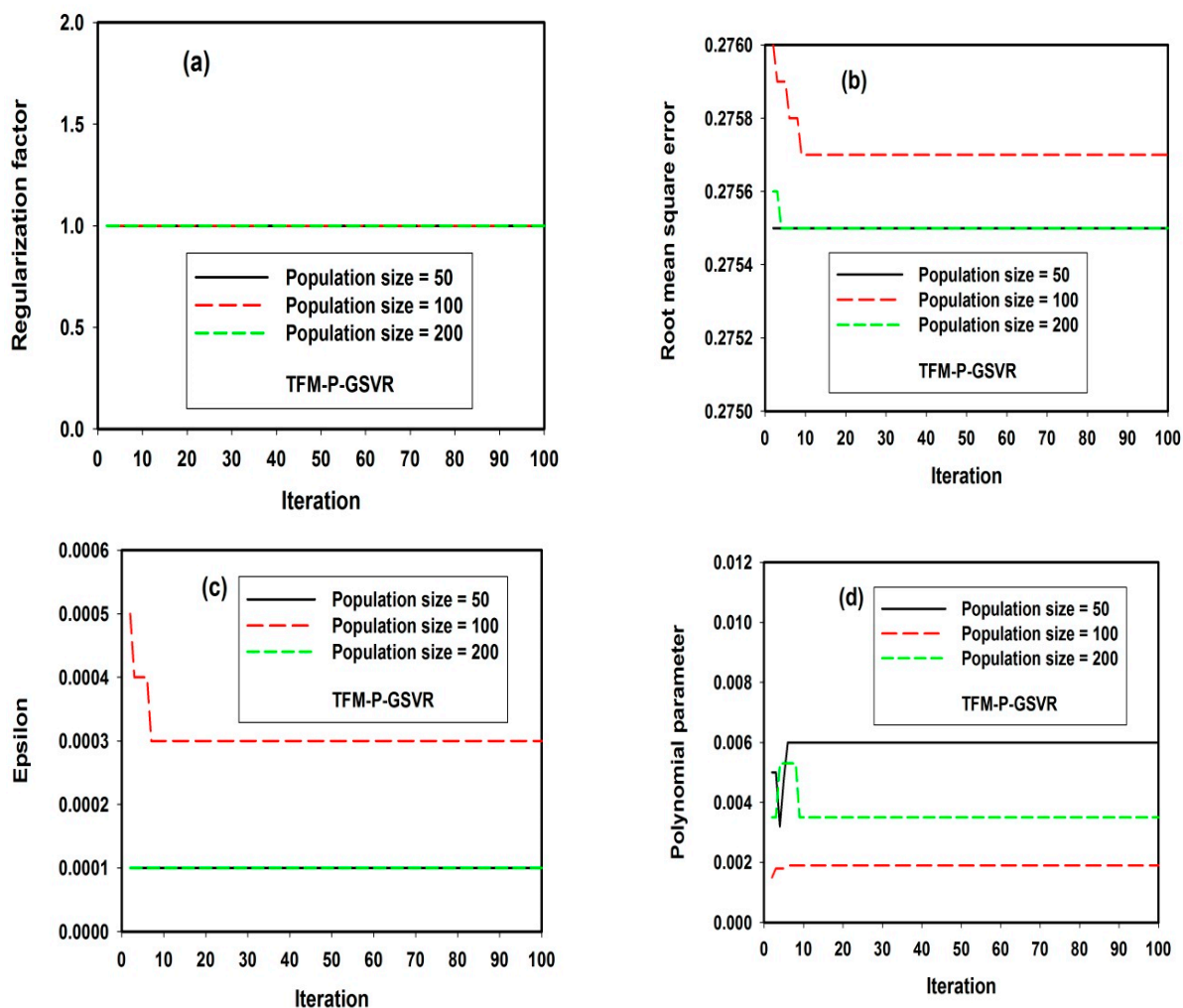


**Figure 4.** Convergence effect of TFM-P-GSVR model on chromosome population size at different iterations: (a) regularization factor; (b) fitness function root mean square error; (c) epsilon error threshold; (d) polynomial mapping parameter.

**Table 2.** Global solutions for TFM-G-GSVR and TFM-P-GSVR models from genetic algorithm implementation.

Parameter	TFM-G-GSVR	TFM-P-GSVR
Regularization factor	1	1
Population size	50	200
Epsilon	0.0001	0.0001
Mapping function	Gaussian	Polynomial
Mapping kernel parameter	30	0.0035

#### 4.2. Performance Assessment Comparison for TFM-G-GSVR and TFM-P-GSVR Models

Assessment parameters were computed on the developed models during the training and testing stages and presented in Figure 5. The assessment parameters employed include the correlation coefficient (CC), mean absolute error (MAE) and root mean square error (RMSE) for both training and testing magnesium-based thermoelectric materials. During the pattern acquisition stage, the computed CCs as presented in Figure 5a for TFM-S-ELM, TFM-G-GSVR, TFM-P-GSVR and TFM-G-ELM models are 1.00, 0.9825, 0.7204 and 0.3548, respectively, with corresponding RMSEs of 0, 0.0845, 0.2987 and 0.4336 as depicted in Figure 5b. Similarly, the obtained MAEs on training thermoelectric samples shown in Figure 5c, for the mentioned TFM-S-ELM, TFM-G-GSVR, TFM-P-GSVR and TFM-G-ELM

models are 0, 0.0341, 0.1888 and 0.3632, respectively. During the implementation of the trained models for validation purposes, the computed CCs presented in Figure 5d for TFM-S-ELM, TFM-G-GSVR, TFM-P-GSVR and TFM-G-ELM models are 0.8198, 0.9597, 0.9598 and 0.9610, respectively while the associated respective values for RMSE are 0.6165, 0.1726, 0.2755 and 0.1262 as depicted in Figure 5e.

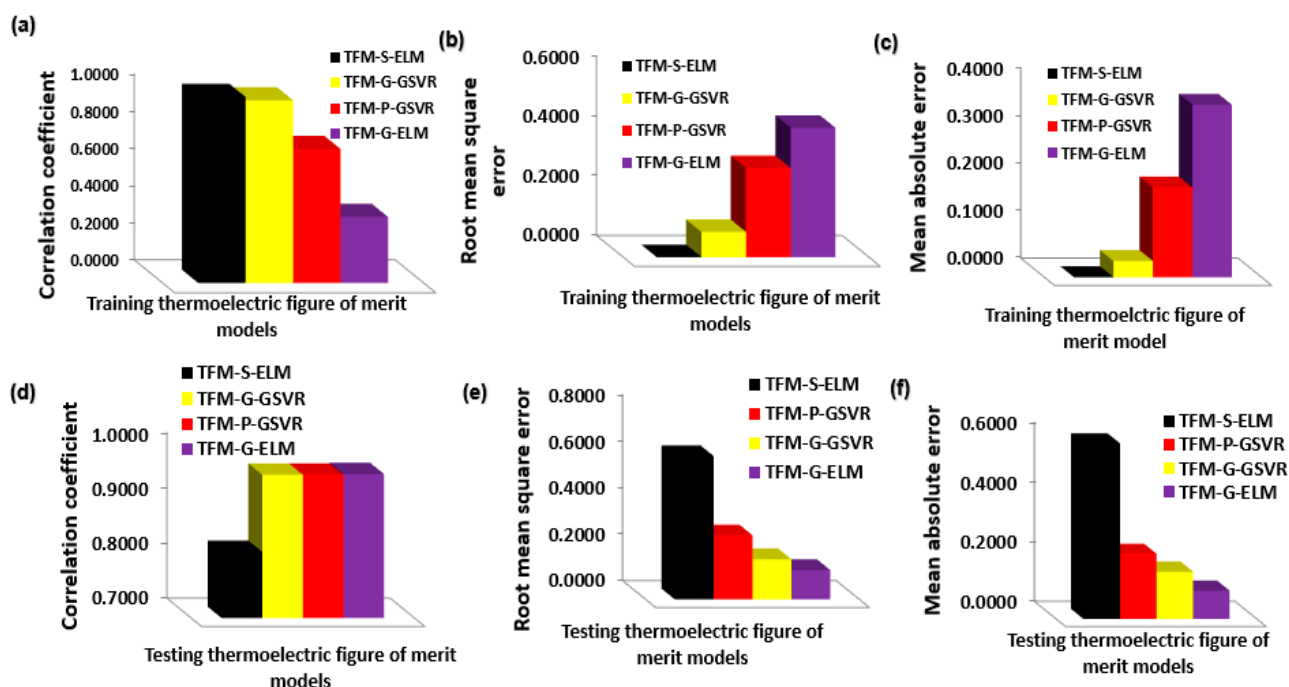


**Figure 5.** Performance assessment comparison of the developed thermoelectric figure of merit models: (a) training samples correlation coefficient; (b) training samples root mean square error; (c) training samples mean absolute error; (d) testing samples correlation coefficient; (e) testing samples root mean square error; (f) testing samples mean absolute error.

For the MAE assessment parameter during the testing phase presented in Figure 5f, values of 0.5889, 0.1588, 0.2187 and 0.0953, respectively, were obtained for TFM-S-ELM, TFM-G-GSVR, TFM-P-GSVR and TFM-G-ELM models. The developed TFM-S-ELM performs better than TFM-G-GSVR, TFM-P-GSVR and TFM-G-ELM models with improvements of 1.70%, 27.96% and 64.52% using CC on training magnesium thermoelectric samples. Additionally, the TFM-G-GSVR model outperforms the TFM-S-ELM model during the testing phase with improvements of 17.06%, 72% and 73.03% using CC, RMSE and MAE assessment metrics, respectively. The developed TFM-P-GSVR also outperforms TFM-S-ELM during the testing stage with improvements of 14.59%, 55.31% and 62.86% using CC, RMSE and MAE assessment metrics, respectively. Also, the developed TFM-G-ELM model shows superiority over the TFM-S-ELM model during the testing stage with improvements of 14.69%, 79.52% and 83.82%, for CC, RMSE and MAE assessment yardsticks, respectively. The developed TFM-G-GSVR model outperforms the TFM-P-GSVR and TFM-G-ELM models during the training stage with respective improvements of 26.68% and 63.89% using the CC metric, 71.71% and 80.51% using the RMSE parameter, 81.94 and 90.61% using MAE assessment factor. However, during the testing phase, TFM-G-GSVR outperforms TFM-P-GSVR with an improvement of 0.01%, while the developed TFM-P-GSVR performs better than the TFM-G-GSVR model with an improvement of 37.35% and 27.39% using RMSE and MAE performance metrics, respectively. The developed TFM-G-ELM outperforms the TFM-G-GSVR model during the testing stage with improvements of 0.13%, 26.85% and 40.01%, using CC, RMSE and MAE parameters, respectively. During the training and pattern acquisition stage, the developed TFM-P-GSVR outperforms the TFM-G-ELM model with improvements of 50.75%, 31.12% and 48.02% using CC, RMSE and MAE assessment

parameters, respectively while the developed TFM-G-ELM model outperforms TFM-P-GSVR model during testing phase with improvements of 0.12%, 54.17% and 56.44%, using respective CC, RMSE and MAE parameters. The assessment parameters for each of the thermoelectric figures of merit models at different modeling stages are shown in Table 3.

**Table 3.** Assessment parameters for the developed thermoelectric figure of merit models.

	Training			Testing		
	CC	RMSE	MAE	CC	RMSE	MAE
TFM-S-ELM	1.0000	0.0000	0.0000	0.8198	0.6165	0.5889
TFM-G-GSVR	0.9825	0.0845	0.0341	0.9597	0.1726	0.1588
TFM-P-GSVR	0.7204	0.2987	0.1888	0.9598	0.2755	0.2187
TFM-G-ELM	0.3548	0.4336	0.3632	0.9610	0.1262	0.0953

Table 4 shows the estimates of each of the developed thermoelectric figures of merit models and the associated absolute errors. The estimates of TFM-G-GSVR model agreed excellently well and exactly with the measured values in the case of  $\text{Mg}_{1.86}\text{Sn}_{0.837}\text{Si}_{0.093}\text{Na}_{0.14}\text{S}_{0.07}$  [61],  $\text{Mg}_2\text{Si}_{0.53}\text{Sn}_{0.4}\text{Ge}_{0.05}\text{Bi}_{0.02}$  [58],  $\text{MgAg}_{0.97}\text{Sb}_{0.99}\text{In}_{0.01}$  [8],  $\text{Mg}_2\text{Si}_{0.6945}\text{Sn}_{0.3}\text{Sb}_{0.0055}$  [58],  $\text{Mg}_{0.97}\text{Zn}_{0.03}\text{Ag}_{0.9}\text{Sb}_{0.95}$  [58] and  $\text{Mg}_2\text{Sn}_{0.8}\text{Sb}_{0.2}$  [58] thermoelectric magnesium-based materials with zero deviation. The developed TFM-G-GSVR model predicts another thermoelectric figure of merit correctly for all the investigated magnesium-based materials with zero deviation from measured values except  $\text{MgAg}_{0.97}\text{Sb}_{0.99}$  [58],  $\text{Mg}_{2.15}\text{Si}_{0.28}\text{Sn}_{0.71}\text{Sb}_{0.006}$  [17],  $\text{Mg}_{0.995}\text{Ca}_{0.005}\text{Ag}_{0.97}\text{Sb}_{0.99}$  [58],  $\text{Mg}_2\text{Si}_{0.6}\text{Ge}_{0.4}\text{Ga}_{0.008}$  [58],  $\text{Mg}_{2.9875}\text{Na}_{0.0125}\text{Sb}_2$  [58],  $\text{Mg}_{2.39}\text{Zn}_{0.6}\text{Ag}_{0.01}\text{Sb}_2$  [60],  $\text{Mg}_{3.2}\text{Sb}_{1.5}\text{Bi}_{0.49}\text{Te}_{0.01}$  [58],  $\text{MgAg}_{0.965}\text{Ni}_{0.005}\text{Sb}_{0.99}$  [58],  $\text{Mg}_{2.1}\text{Si}_{0.38}\text{Sn}_{0.6}\text{Sb}_{0.02}$  [58],  $\text{Mg}_{1.95}\text{Na}_{0.01}\text{ZnSb}_2$  [14] and  $\text{Mg}_{3.5}\text{Te}_{0.03}\text{Sb}_{1.97}\text{Te}_{0.03}$  [4] that have slight deviations from the measured values.

The developed TFM-P-GSVR model gives the thermoelectric figure of merit of some thermoelectric magnesium materials exactly when compared with the measured values while estimates of other compounds have characteristics insignificant deviations. Magnesium-based compounds with exact predictions using TFM-P-GSVR include  $\text{Mg}_{1.86}\text{Sn}_{0.837}\text{Si}_{0.093}\text{Na}_{0.14}\text{S}_{0.07}$  [61],  $\text{Mg}_{1.86}\text{Li}_{0.14}\text{Si}_{0.3}\text{Sn}_{0.7}$  [59] and  $\text{Mg}_{1.95}\text{Li}_{0.05}\text{Ge}$  [9] among others. The estimates of the majority of magnesium-based thermoelectric materials predicted by the TFM-S-ELM model agree exactly with the measured values while the predictions of the developed TFM-G-ELM model have associated deviations from the measured values. The developed TFM-G-GSVR has the lowest mean absolute percentage error (MAPE) of 0.06 as shown in Table 4 followed by the TFM-S-ELM model with a value of 0.12, TFM-P-GSVR with a value of 0, and TFM-G-ELM model, which has a 0.31 MAPE.

**Table 4.** Estimates of the developed thermoelectric figure of merit models and the associated absolute error.

Compound	Temp (K)	Measured TFM	TFM-G-GSVR	Error	TFM-P-GSVR	Error	TFM-S-ELM	Error	TFM-G-ELM	Error
$\text{Mg}_{1.86}\text{Sn}_{0.837}\text{Si}_{0.093}\text{Na}_{0.14}\text{S}_{0.07}$	673	0.52 [61]	0.52	0.00	0.52	0.00	0.52	0.00	1.27	0.75
$\text{Mg}_2\text{Si}_{0.53}\text{Sn}_{0.4}\text{Ge}_{0.05}\text{Bi}_{0.02}$	800	1.40 [58]	1.40	0.00	1.39	0.01	1.40	0.00	1.25	0.15
$\text{MgAg}_{0.97}\text{Sb}_{0.99}\text{In}_{0.01}$	525	1.10 [8]	1.10	0.00	1.29	0.19	1.10	0.00	1.23	0.13
$\text{Mg}_2\text{Si}_{0.6945}\text{Sn}_{0.3}\text{Sb}_{0.0055}$	620	0.55 [58]	0.55	0.00	0.92	0.37	0.55	0.00	0.90	0.35
$\text{Mg}_{0.97}\text{Zn}_{0.03}\text{Ag}_{0.9}\text{Sb}_{0.95}$	423	1.40 [58]	1.40	0.00	1.12	0.28	1.40	0.00	1.25	0.15
$\text{Mg}_2\text{Sn}_{0.8}\text{Sb}_{0.2}$	750	0.90 [58]	0.90	0.00	0.35	0.55	0.12	0.78	0.89	0.01
$\text{MgAg}_{0.97}\text{Sb}_{0.99}$	450	1.20 [58]	1.03	0.17	0.83	0.37	1.20	0.00	1.15	0.05
$\text{Mg}_{2.15}\text{Si}_{0.28}\text{Sn}_{0.71}\text{Sb}_{0.006}$	700	1.30 [17]	1.14	0.16	0.87	0.43	1.30	0.00	0.89	0.41
$\text{Mg}_{0.995}\text{Ca}_{0.005}\text{Ag}_{0.97}\text{Sb}_{0.99}$	525	1.30 [58]	1.06	0.24	1.35	0.05	1.72	0.42	1.23	0.07
$\text{Mg}_{1.86}\text{Li}_{0.14}\text{Si}_{0.3}\text{Sn}_{0.7}$	750	0.50 [59]	0.50	0.00	0.50	0.00	0.50	0.00	0.89	0.39
$\text{Mg}_{2.4875}\text{Zn}_{0.5}\text{Na}_{0.0125}\text{Sb}_2$	773	0.80 [54]	0.80	0.00	0.97	0.17	0.10	0.70	0.89	0.09
$\text{Mg}_2\text{Si}_{0.6}\text{Ge}_{0.4}\text{Ga}_{0.008}$	625	0.36 [58]	0.60	0.24	0.88	0.52	0.36	0.00	0.89	0.53
$\text{Mg}_{2.9875}\text{Na}_{0.0125}\text{Sb}_2$	773	0.60 [58]	0.69	0.09	0.80	0.20	0.60	0.00	0.89	0.29
$\text{Mg}_{1.95}\text{Li}_{0.05}\text{Ge}$	700	0.50 [9]	0.50	0.00	0.50	0.00	0.50	0.00	0.89	0.39
$\text{Mg}_{0.99}\text{Li}_{0.01}\text{Ag}_{0.97}\text{Sb}_{0.99}$	525	1.25 [58]	1.25	0.00	1.25	0.00	1.25	0.00	1.23	0.02

Table 4. Cont.

Compound	Temp (K)	Measured TFM	TFM-G-GSVR	Error	TFM-P-GSVR	Error	TFM-S-ELM	Error	TFM-G-ELM	Error
Mg <sub>1.95</sub> Ag <sub>0.05</sub> Si <sub>0.4</sub> Sn <sub>0.6</sub>	690	0.45 [55]	0.45	0.00	0.70	0.25	0.45	0.00	0.89	0.44
Mg <sub>2.39</sub> Zn <sub>0.6</sub> Ag <sub>0.01</sub> Sb <sub>2</sub>	773	0.84 [60]	0.78	0.06	0.89	0.05	0.09	0.75	0.89	0.05
Mg <sub>3.2</sub> Sb <sub>1.5</sub> Bi <sub>0.49</sub> Te <sub>0.01</sub>	700	1.50 [58]	1.42	0.08	1.58	0.08	1.50	0.00	0.92	0.58
MgAg <sub>0.965</sub> Ni <sub>0.005</sub> Sb <sub>0.99</sub>	450	1.40 [58]	1.17	0.23	0.44	0.96	1.12	0.28	1.32	0.08
Mg <sub>3.07</sub> Sb <sub>1.5</sub> Bi <sub>0.48</sub> Se <sub>0.02</sub>	725	1.23 [15]	1.23	0.00	1.23	0.00	1.23	0.00	0.89	0.34
Mg <sub>2.85</sub> Cd <sub>0.5</sub> Sb <sub>2</sub>	773	0.75 [13]	0.75	0.00	0.75	0.00	0.75	0.00	0.89	0.14
Mg <sub>2.85</sub> Sn <sub>0.6</sub> Sb <sub>0.02</sub>	700	0.85 [58]	1.06	0.21	0.85	0.00	0.85	0.00	0.89	0.04
Mg <sub>3.5</sub> Nd <sub>0.04</sub> Sb <sub>1.97</sub> Te <sub>0.03</sub>	775	1.65 [4]	1.65	0.00	1.65	0.00	1.65	0.00	0.89	0.76
Mg <sub>3.15</sub> Mn <sub>0.05</sub> Sb <sub>1.5</sub> Bi <sub>0.49</sub> Se <sub>0.01</sub>	623	1.70 [56]	1.70	0.00	1.47	0.23	1.70	0.00	1.25	0.45
Mg <sub>3.5</sub> Sc <sub>0.04</sub> Sb <sub>1.97</sub> Te <sub>0.03</sub>	725	1.50 [58]	1.50	0.00	1.50	0.00	0.90	0.60	1.23	0.27
Mg <sub>3.032</sub> Y <sub>0.018</sub> SbBi	700	1.80 [58]	1.80	0.00	1.49	0.31	1.80	0.00	1.23	0.57
Mg <sub>2.985</sub> Ag <sub>0.015</sub> Sb <sub>2</sub>	725	0.51 [6]	0.51	0.00	0.84	0.33	0.51	0.00	0.89	0.38
Mg <sub>2.15</sub> Sm <sub>0.5</sub> Ca <sub>0.5</sub> Bi <sub>1.99</sub> Ge <sub>0.01</sub>	873	0.71 [57]	0.71	0.00	1.01	0.30	0.71	0.00	1.23	0.52
Mg <sub>1.95</sub> Na <sub>0.01</sub> ZnSb <sub>2</sub>	773	0.87 [14]	0.90	0.03	0.87	0.00	0.87	0.00	0.89	0.02
Mg <sub>3.5</sub> Tm <sub>0.03</sub> Sb <sub>1.97</sub> Te <sub>0.03</sub>	775	1.75 [4]	1.50	0.25	1.54	0.21	1.75	0.00	0.89	0.86
Mean absolute percentage error (MAPE)				0.06		0.19		0.12		0.31

#### 4.3. Influence of Temperature and Dopant Concentration on Magnesium-Based Thermoelectric Materials Using Developed TFM-P-SVR Model

The dependence of the thermoelectric figure of merit of Mg<sub>2.1</sub>Si<sub>0.38</sub>Sn<sub>0.6-x</sub>Sb<sub>x</sub> material is investigated using the TFM-P-GSVR model and shown in Figure 6. The significance of antimony (Sb) dopant in adjusting the figure of merit of Mg<sub>2.1</sub>Si<sub>0.38</sub>Sn<sub>0.6-x</sub>Sb<sub>x</sub> magnesium-based thermoelectric compound is also deduced from Figure 6.

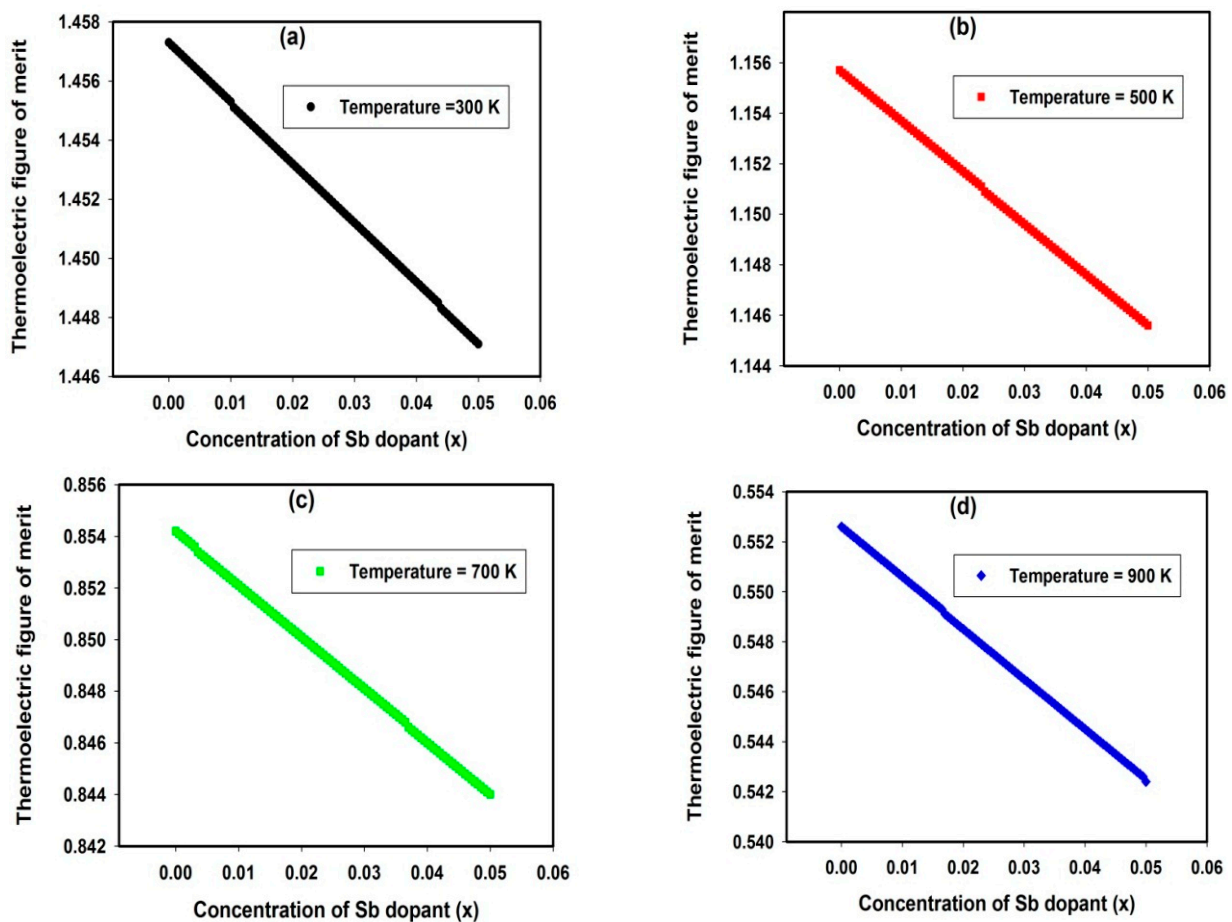
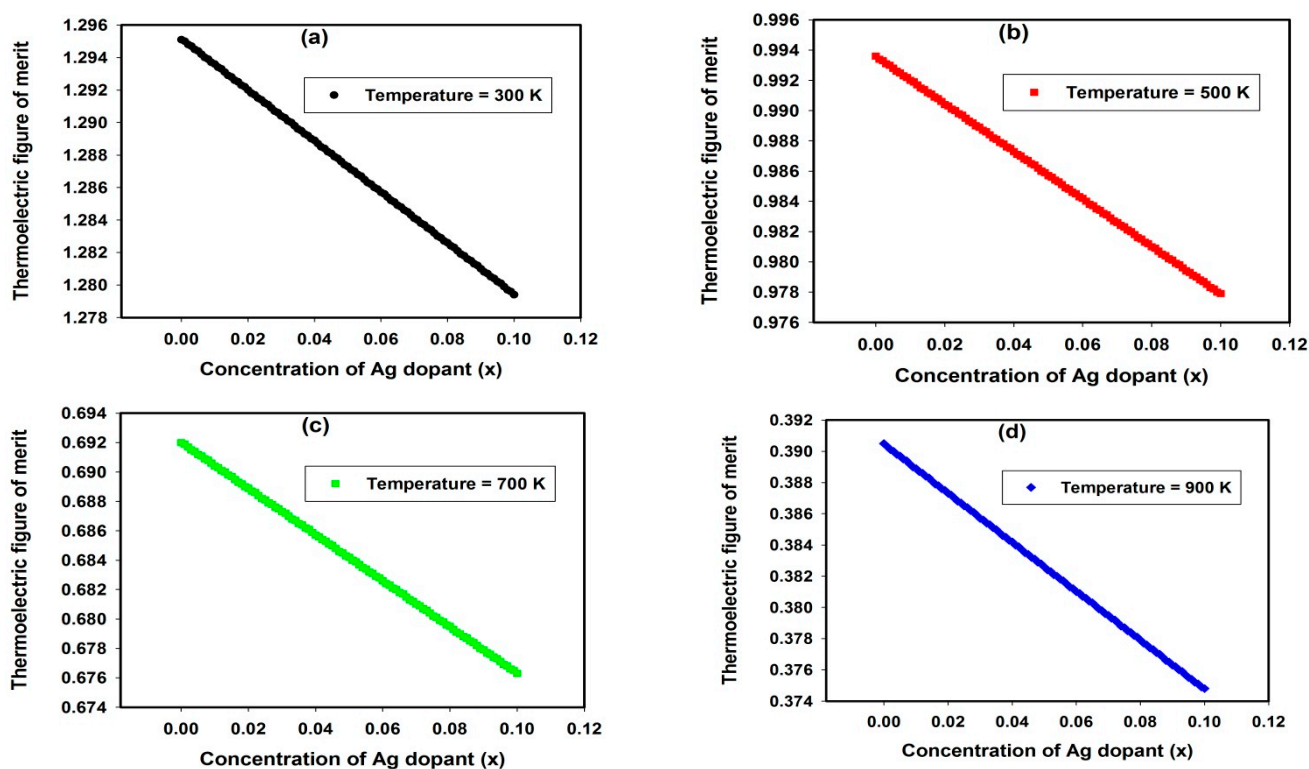


Figure 6. Temperature dependent on thermoelectric figure of merit for Mg<sub>2.1</sub>Si<sub>0.38</sub>Sn<sub>0.6-x</sub>Sb<sub>x</sub> material at (a) 300 K (b) 500 K (c) 700 K and (d) 900 K.

Figure 6a,b, respectively, present how the antimony (Sb) substitution for tin (Sn) particles in crystallography of Mg<sub>2.1</sub>Si<sub>0.38</sub>Sn<sub>0.6-x</sub>Sb<sub>x</sub> material influences the thermoelectric

figure of merit for 300 K and 500 K operating temperature. Figure 6c,d show the alteration of the thermoelectric figure of merit for 700 K and 900 K operating temperatures, respectively. An increase in the concentration of antimony in  $\text{Mg}_{2.1}\text{Si}_{0.38}\text{Sn}_{0.6-x}\text{Sb}_x$  material lowers the thermoelectric figure of merit. The temperature has a similar thermoelectric figure-of-merit-lowering influence on  $\text{Mg}_{2.1}\text{Si}_{0.38}\text{Sn}_{0.6-x}\text{Sb}_x$  magnesium-based materials. A similar value of the thermoelectric figure of merit has been reported experimentally for the  $\text{Mg}_{2.1}\text{Si}_{0.38}\text{Sn}_{0.6}\text{Sb}_{0.02}$  compound at a temperature of 700 K [58]. It should be noted that the presented trend and prediction employ the support vector saved during the model training, allowing the deployment of the models to adjust the thermoelectric figure of merit of magnesium-based compounds to the desired value. Another uniqueness of the developed model is the possibility of incorporating four different elements into the compound at different concentrations. This widens the possibility of exploring varieties of elements in the periodic table for attaining improved thermoelectric figures of merit. A similar influence is obtained for the  $\text{Mg}_{2-x}\text{Ag}_x\text{Si}_{0.4}\text{Sn}_{0.6}$  material presented in Figure 7. The significance of silver (Ag) incorporation at 300 K (as shown in Figure 7a), 500 K (as presented in Figure 7b), 700 K (as depicted by Figure 7c) and 900 K (as shown in Figure 7d) is investigated using the developed TFM-P-GSVR model.



**Figure 7.** Temperature dependent on thermoelectric figure of merit for  $\text{Mg}_{2-x}\text{Ag}_x\text{Si}_{0.4}\text{Sn}_{0.6}$  material at (a) 300 K (b) 500 K (c) 700 K and (d) 900 K.

An increase in both temperature and silver concentration lowers the thermoelectric figure of merit for the  $\text{Mg}_{2-x}\text{Ag}_x\text{Si}_{0.4}\text{Sn}_{0.6}$  material. However, the doped silver-doped thermoelectric material has a lower thermoelectric figure of merit at different temperatures as compared with the antimony-doped magnesium thermoelectric material. Similar behavior has been reported experimentally for the  $\text{Mg}_{1.95}\text{Ag}_{0.05}\text{Si}_{0.4}\text{Sn}_{0.6}$  compound at 690 K [55].

## 5. Conclusions

Thermoelectric figure of merit (TFM) for magnesium-based thermoelectric materials is modeled through extreme learning machine (ELM) and hybrid genetic-based algorithm-based support vector regression (GSVR) algorithms using operating temperature, ionic

radii of elemental compositions and elemental concentrations. The mapping functions employed in the GSVR-based model include the Gaussian (G) and polynomial (P), while sine (S) and sigmoid function (G) activation functions were utilized for ELM-based models. The developed TFM-G-GSVR model outperforms the TFM-P-GSVR and TFM-G-ELM models during the training stage with respective improvements of 26.68% and 63.89% using the CC metric, 71.71% and 80.51% using the RMSE parameter, and 81.94 and 90.61% using the MAE assessment factor. However, during the testing phase, TFM-G-GSVR outperforms TFM-P-GSVR with an improvement of 0.01%, while the developed TFM-P-GSVR performs better than the TFM-G-GSVR model with an improvement of 37.35% and 27.39% using RMSE and MAE performance metrics, respectively. The developed TFM-G-ELM outperforms the TFM-G-GSVR model with improvements of 0.13%, 26.85% and 40.01%, using CC, RMSE and MAE parameters, respectively. The predictions of the developed models align excellently with the measured values. Thermoelectric figures of merit for some magnesium-based thermoelectric materials were investigated using the developed model and the obtained trend aligns with the reported experimental patterns. The uniqueness of the developed intelligent models in incorporating four different elements into the chemical structure of magnesium-based thermoelectric materials coupled with impressive performance would strengthen the wider exploration of magnesium thermoelectric materials for desired industrial and technological applications for bringing the global energy crisis under control.

**Supplementary Materials:** The following supporting information can be downloaded at: <https://www.mdpi.com/article/10.3390/inorganics12030085/s1>, The MATLAB source codes for the developed GSVR-based models are included as supplementary material. Extracted weights in Excel format for reproducing ELM-based models are also attached.

**Funding:** This research received no external funding.

**Data Availability Statement:** The raw data required to reproduce these findings are available in the cited references in Section 3.1 of the manuscript.

**Conflicts of Interest:** The authors declare no conflicts of interest.

## References

1. Yin, Z.; Liu, Z.; Yu, Y.; Zhang, C.; Chen, P.; Zhao, J.; He, P.; Guo, X. Synergistically Optimized Electron and Phonon Transport of Polycrystalline BiCuSeO via Pb and Yb Co-Doping. *Appl. Mater. Interfaces* **2021**, *13*, 57638–57645. [[CrossRef](#)] [[PubMed](#)]
2. Novitskii, A.; Serhienko, I.; Novikov, S.; Kuskov, K.; Pankratova, D.; Sviridova, T.; Voronin, A.; Bogach, A.; Skryleva, E.; Parkhomenko, Y.; et al. Correlation between structural and transport properties of electron beam irradiated PrMnO<sub>3</sub> compounds. *Solid State Commun.* **2018**, *270*, 30–37.
3. Sviridova, T.; Voronin, A.; Bogach, A.; Skryleva, E.; Parkhomenko, Y. Thermoelectric properties of Sm-doped BiCuSeO oxyseLENIDES fabricated by two-step reactive sintering. *J. Alloys Compd.* **2022**, *912*, 165208.
4. Zhang, J.; Song, L.; Iversen, B.B. Probing Efficient N-Type Lanthanide Dopants for Mg<sub>3</sub>Sb<sub>2</sub> Thermoelectrics. *Adv. Sci.* **2020**, *7*, 2002867. [[CrossRef](#)]
5. Liu, Z.; Wang, Y.; Gao, W.; Mao, J.; Geng, H.; Shuai, J.; Cai, W.; Sui, J.; Ren, Z. The influence of doping sites on achieving higher thermoelectric performance for nanostructured  $\alpha$ -MgAgSb. *Nano Energy* **2017**, *31*, 194–200. [[CrossRef](#)]
6. Song, L.; Zhang, J.; Iversen, B.B. Simultaneous improvement of power factor and thermal conductivity via Ag doping in p-type Mg<sub>3</sub>Sb<sub>2</sub> thermoelectric materials. *J. Mater. Chem. A* **2017**, *5*, 4932–4939. [[CrossRef](#)]
7. Feng, B.; Li, G.; Pan, Z.; Hu, X.; Liu, P.; He, Z. Enhanced thermoelectric performance in BiCuSeO oxyselenides via Ba/Te dual-site substitution and 3D modulation doping. *J. Solid State Chem.* **2018**, *266*, 297–303. [[CrossRef](#)]
8. Ying, P.; Liu, X.; Fu, C.; Yue, X.; Xie, H.; Zhao, X.; Zhang, W.; Zhu, T. High Performance  $\alpha$ -MgAgSb Thermoelectric Materials for Low Temperature Power Generation. *Chem. Mater.* **2015**, *27*, 909–913. [[CrossRef](#)]
9. Kamila, H.; Sankhla, A.; Yasserli, M.; Mueller, E. Non-Rigid Band Structure in Mg<sub>2</sub>Ge for Improved Thermoelectric Performance. *Adv. Sci.* **2020**, *7*, 2000070. [[CrossRef](#)]
10. Santos, R.; Yamini, S.A.; Dou, S.X. Recent progress in magnesium-based thermoelectric materials. *J. Mater. Chem. A* **2018**, *6*, 3328–3341. [[CrossRef](#)]
11. Han, G.; Lu, Y.; Jia, H.; Ding, Z.; Wu, L.; Shi, Y.; Wang, G.; Luo, Q.; Wang, J.; Huang, G.; et al. Magnesium-based energy materials: Progress, challenges, and perspectives. *J. Magnes. Alloys* **2023**, *11*, 3896–3925. [[CrossRef](#)]

12. Li, A.; Fu, C.; Zhao, X.; Zhu, T. High-Performance  $\text{Mg}_3\text{Sb}_{2-x}\text{Bi}_x$  Thermoelectrics: Progress and Perspective. *Research* **2020**, *2020*, 1934848. [[CrossRef](#)]
13. Xiao, S.; Peng, K.; Zhou, Z.; Wang, H.; Zheng, S.; Lu, X.; Han, G.; Wang, G.; Zhou, X. Realizing Cd and Ag codoping in p-type  $\text{Mg}_3\text{Sb}_2$  toward high thermoelectric performance. *J. Magnes. Alloys* **2023**, *11*, 2486–2494. [[CrossRef](#)]
14. Hu, J.; Zhu, J.; Guo, F.; Qin, H.; Liu, Y.; Zhang, Q.; Liu, Z.; Cai, W.; Sui, J. Electronic Orbital Alignment and Hierarchical Phonon Scattering Enabling High Thermoelectric Performance p-Type  $\text{Mg}_3\text{Sb}_2$  Zintl Compounds. *AAAS Res.* **2022**, *2022*, 9842949.
15. Zhang, J.; Song, L.; Mamakhel, A.; Ry, M.; Jørgensen, V. High-Performance Low-Cost n-Type Se-Doped  $\text{Mg}_3\text{Sb}_2$ -Based Zintl Compounds for Thermoelectric Application. *Chem. Mater.* **2017**, *29*, 5371–5383. [[CrossRef](#)]
16. Tamaki, H.; Sato, H.K.; Kanno, T. Isotropic Conduction Network and Defect Chemistry in  $\text{Mg}_{3+\delta}\text{Sb}_2$ -Based Layered Zintl Compounds with High Thermoelectric Performance. *Adv. Mater.* **2016**, *01*, 10182–10187. [[CrossRef](#)] [[PubMed](#)]
17. Liu, W.; Tan, X.; Yin, K.; Liu, H.; Tang, X.; Shi, J.; Zhang, Q.; Uher, C. Convergence of Conduction Bands as a Means of Enhancing Thermoelectric Performance of n-Type  $\text{Mg}_2\text{Si}_{1-x}\text{Sn}_x$  Solid Solutions. *Phys. Rev. Lett.* **2012**, *108*, 166601. [[CrossRef](#)]
18. Xin, J.; Zhang, Y.; Wu, H.; Zhu, T.; Fu, T.; Shen, J.; Pennycook, S.J.; Zhao, X. Multiscale Defects as Strong Phonon Scatters to Enhance Thermoelectric Performance in  $\text{Mg}_2\text{Sn}_{1-x}\text{Sb}_x$  Solid Solutions. *Small Methods* **2019**, *3*, 1900412. [[CrossRef](#)]
19. Murillo-Escobar, J.; Sepulveda-Suescun, J.P.; Correa, M.A.; Orrego-Metaute, D. Urban Climate Forecasting concentrations of air pollutants using support vector regression improved with particle swarm optimization: Case study in Aburrá Valley, Colombia. *Urban Clim.* **2019**, *29*, 100473. [[CrossRef](#)]
20. Zhang, Z.; Ding, S.; Sun, Y. Neurocomputing A support vector regression model hybridized with chaotic krill herd algorithm and empirical mode decomposition for regression task. *Neurocomputing* **2020**, *410*, 185–201. [[CrossRef](#)]
21. Owolabi, T.O. Modeling magnetocaloric effect of doped  $\text{EuTiO}_3$  perovskite for cooling technology using swarm intelligent based support vector regression computational method. *Mater. Today Commun.* **2023**, *36*, 106688. [[CrossRef](#)]
22. Owolabi, T.O.; Akande, K.O.; Olatunji, S.O. Estimation of Superconducting Transition Temperature  $T_c$  for Superconductors of the Doped  $\text{MgB}_2$  System from the Crystal Lattice Parameters Using Support Vector Regression. *J. Supercond. Nov. Magn.* **2014**, *28*, 75–81. [[CrossRef](#)]
23. Owolabi, T.O.; Akande, K.O.; Olatunji, S.O. Estimation of average surface energies of transition metal nitrides using computational intelligence technique. *Soft Comput.* **2017**, *21*, 20. [[CrossRef](#)]
24. Owolabi, T.O.; Akande, K.O.; Olatunji, S.O. Application of computational intelligence technique for estimating superconducting transition temperature of YBCO superconductors. *Appl. Soft Comput.* **2016**, *43*, 143–149. [[CrossRef](#)]
25. Zhang, Z.; Liu, S.; Zhang, Y.; Wang, C.; Zhang, S.; Yang, Z. Optimization of low-power femtosecond laser trepan drilling by machine learning and a high-throughput multi-objective genetic algorithm. *Opt. Laser Technol.* **2021**, *148*, 107688. [[CrossRef](#)]
26. Okoye, P.C.; Azi, S.O.; Owolabi, T.O.; Adeyemi, O.W.; Souiyah, M.; Latif, M.B.; Olusayo, O. Modeling Energy Gap of Doped Tin (II) Sulfide Metal Semiconductor Nanocatalyst Using Genetic Algorithm-Based Support Vector Regression. *J. Nanomater.* **2022**, *2022*, 8211023. [[CrossRef](#)]
27. Israel, E.E.; Adamu, U.; Eyije, A.S. Multi-Target In-Silico Study of 5,6-Dihydro-2-Pyrones, Indole B-Diketo Acid, Diketo Acid and Carboxamide Derivatives against Various Anti-HIV-1 Strain at PM3 Semi-Empirical Level. *Ewemen J. Pharm.* **2016**, *1*, 1–13.
28. Shi, Q.; Niu, G.; Lin, Q.; Xu, T.; Li, F.; Duan, Y. Quantitative analysis of sedimentary rocks using laser-induced breakdown spectroscopy: Comparison of support vector regression and partial least squares regression chemometric methods. *J. Anal. At. Spectrom.* **2015**, *30*, 2384–2393. [[CrossRef](#)]
29. Do, H.T.; Van Bach, N.; Van Nguyen, L.; Tran, H.T.; Nguyen, M.T. A design of higher-level control based genetic algorithms for wastewater treatment plants. *Eng. Sci. Technol. Int. J.* **2021**, *24*, 872–878. [[CrossRef](#)]
30. Owolabi, T.O.; Gondal, M.A. Development of hybrid extreme learning machine based chemo-metrics for precise quantitative analysis of LIBS spectra using internal reference pre-processing method. *Anal. Chim. Acta* **2018**, *1030*, 33–41. [[CrossRef](#)]
31. Alqahtani, A. Engineering the Energy Gap of Cupric Oxide Nanomaterial Using Extreme Learning Machine and Stepwise Regression Algorithms. *J. Nanomater.* **2021**, *2021*, 4797686. [[CrossRef](#)]
32. Owolabi, T.O. Extreme learning machine and swarm-based support vector regression methods for predicting crystal lattice parameters of pseudo-cubic/cubic perovskites Extreme learning machine and swarm-based support vector regression methods for predicting crystal lat. *J. Appl. Phys.* **2020**, *127*, 245107. [[CrossRef](#)]
33. Cao, Y.; Wakil, K.; Alyousef, R.; Jermisittiparsert, K.; Si, L. Application of extreme learning machine in behavior of beam to column connections. *Structures* **2020**, *25*, 861–867. [[CrossRef](#)]
34. Shamsah, S.M.I.; Owolabi, T.O. Newtonian mechanics based hybrid machine learning method of characterizing energy band gap of doped zno semiconductor. *Chin. J. Phys.* **2020**, *68*, 493–506. [[CrossRef](#)]
35. Vapnik, V.N. *Statistical Learning Theory*; Wiley-Interscience: New York, NY, USA, 1998.
36. Akomolafe, O.; Owolabi, T.O.; Rahman, M.A.A.; Kechik, M.M.A.; Yasin, M.N.M.; Souiyah, M. Modeling superconducting critical temperature of 122-iron-based pnictide intermetallic superconductor using a hybrid intelligent computational method. *Materials* **2021**, *14*, 4604. [[CrossRef](#)] [[PubMed](#)]
37. Shamsah, S.M.I.; Owolabi, T.O. Modeling the Maximum Magnetic Entropy Change of Doped Manganite Using a Grid Search-Based Extreme Learning Machine and Hybrid Gravitational Search-Based Support Vector Regression. *Crystals* **2020**, *10*, 310. [[CrossRef](#)]

38. Owolabi, T.O.; Amiruddin, M.; Rahman, A. Prediction of Band Gap Energy of Doped Graphitic Carbon Nitride Using Genetic Algorithm-Based Support Vector Regression and Extreme Learning Machine. *Symmetry* **2021**, *13*, 411. [[CrossRef](#)]
39. Owolabi, T.O.; Amiruddin, M.; Rahman, A. Energy Band Gap Modeling of Doped Bismuth Ferrite Multifunctional Material Using Gravitational Search Algorithm Optimized Support Vector Regression. *Crystals* **2021**, *11*, 246. [[CrossRef](#)]
40. Huang, G.B.; Zhu, Q.Y.; Siew, C.K. Extreme learning machine: Theory and applications. *Neurocomputing* **2006**, *70*, 489–501. [[CrossRef](#)]
41. Owolabi, T.O.; Gondal, M.A. Quantitative analysis of LIBS spectra using hybrid chemometric models through fusion of extreme learning machines and support vector regression. *J. Intell. Fuzzy Syst.* **2018**, *35*, 6277–6286. [[CrossRef](#)]
42. Oyenyin, O.E.; Obadawo, B.S.; Olanrewaju, A.A.; Owolabi, T.O.; Gbadamosi, F.A.; Ipinloju, N.; Modamori, H.O. Predicting the bioactivity of 2-alkoxycarbonylallyl esters as potential antiproliferative agents against pancreatic cancer (MiaPaCa-2) cell lines: GFA-based QSAR and ELM-based models with molecular docking. *J. Genet. Eng. Biotechnol.* **2021**, *19*, 38. [[CrossRef](#)]
43. Alqahtani, A.; Saliu, S.; Owolabi, T.O.; Aldhafferi, N.; Almurayh, A.; Oyenyin, O.E. Modeling the magnetic cooling efficiency of spinel ferrite magnetocaloric compounds for magnetic refrigeration application using hybrid intelligent computational methods. *Mater. Today Commun.* **2022**, *33*, 104310. [[CrossRef](#)]
44. Zhao, Y.; Chen, Y. Extreme learning machine based transfer learning for aero engine fault diagnosis. *Aerosp. Sci. Technol.* **2022**, *121*, 107311. [[CrossRef](#)]
45. Agbi, J.I.; Owolabi, T.O.; Abajiigin, D.D. Exploration and quantification of magnetocaloric effect in EuTiO<sub>3</sub> perovskite using extreme learning machine intelligent computational method. *Mater. Today Commun.* **2023**, *37*, 107297. [[CrossRef](#)]
46. Yan, J.; Chen, F.; Liu, T.; Zhang, Y.; Peng, X.; Yi, D. Knowledge-Based Systems Subspace alignment based on an extreme learning machine for electronic nose drift compensation. *Knowl. Based Syst.* **2022**, *235*, 107664. [[CrossRef](#)]
47. Olubosede, O.; Abd Rahman, M.A.; Alqahtani, A.; Souiyah, M.; Latif, M.B.; Oke, W.A.; Aldhafferi, N.; Owolabi, T.O. Tailoring the Energy Harvesting Capacity of Zinc Selenide Semiconductor Nanomaterial through Optical Band Gap. *Crystals* **2022**, *12*, 36. [[CrossRef](#)]
48. Oke, W.A.; Aldhafferi, N.; Saliu, S.; Owolabi, T.O.; Alqahtani, A.; Almurayh, A.; Qahtan, T.F. Modeling the magnetocaloric effect of spinel ferrites for magnetic refrigeration technology using extreme learning machine and genetically hybridized support vector regression computational methods. *Cogent Eng.* **2023**, *10*, 2257955. [[CrossRef](#)]
49. Owolabi, T.O. Determination of the Velocity of Detonation of Primary Explosives using Genetically Optimized Support Vector Regression. *Propellants Explos. Pyrotech.* **2019**, *44*, 1282–1292. [[CrossRef](#)]
50. Dodangeh, E.; Panahi, M.; Rezaie, F.; Lee, S.; Tien, D. Novel hybrid intelligence models for flood-susceptibility prediction: Meta optimization of the GMDH and SVR models with the genetic algorithm and harmony search. *J. Hydrol.* **2020**, *590*, 125423. [[CrossRef](#)]
51. Liang, G.; Xu, J.; Liu, L. QSPR analysis for melting point of fatty acids using genetic algorithm based multiple linear regression (GA-MLR). *Fluid Phase Equilibria* **2013**, *353*, 15–21. [[CrossRef](#)]
52. Nili-Ahmadabadi, M.; Aghabozorgi, F.; Cho, D.S.; Kim, K.C. Development and validation of a hybrid aerodynamic design method for curved diffusers using genetic algorithm and ball-spine inverse design method. *Alex. Eng. J.* **2021**, *60*, 3021–3036. [[CrossRef](#)]
53. Al-Sodani, K.A.A.; Adewumi, A.A.; Mohd Ariffin, M.A.; Maslehuddin, M.; Ismail, M.; Salami, H.O.; Owolabi, T.O.; Mohamed, H.D. Experimental and modelling of alkali-activated mortar compressive strength using hybrid support vector regression and genetic algorithm. *Materials* **2021**, *14*, 3049. [[CrossRef](#)] [[PubMed](#)]
54. Ren, Z.; Shuai, J.; Mao, J.; Zhu, Q.; Song, S.; Ni, Y. Significantly enhanced thermoelectric properties of p-type Mg<sub>3</sub>Sb<sub>2</sub> via co-doping of Na and Zn. *Acta Mater.* **2018**, *143*, 265–271. [[CrossRef](#)]
55. Tang, X.; Zhang, Y.; Zheng, Y.; Peng, K.; Huang, T.; Lu, X.; Wang, G.; Wang, S.; Zhou, X. Improving thermoelectric performance of p-type Ag-doped Mg<sub>2</sub>Si<sub>0.4</sub>Sn<sub>0.6</sub> prepared by unique melt spinning method. *Appl. Therm. Eng.* **2017**, *111*, 1396–1400. [[CrossRef](#)]
56. Zhang, F.; Chen, C.; Yao, H.; Bai, F.; Yin, L.; Li, X.; Li, S.; Xue, W.; Wang, Y.; Cao, F.; et al. High-Performance N-type Mg<sub>3</sub>Sb<sub>2</sub> towards Thermoelectric Application near Room Temperature. *Adv. Funct. Mater.* **2020**, *30*, 1906143. [[CrossRef](#)]
57. Huo, Y.; Xiao, S.; Dai, L.; Huang, Y.; Zheng, S.; Wang, Z.; Chen, P.; Han, G.; Lu, X.; Zhou, X.; et al. Enhanced Thermoelectric Performance in SmMg<sub>2</sub>Bi<sub>2</sub> via Ca-Alloying and Ge-Doping. *Appl. Energy Mater.* **2022**, *5*, 5182–5190. [[CrossRef](#)]
58. Zhou, Z.; Han, G.; Lu, X.; Wang, G.; Zhou, X. High-performance magnesium-based thermoelectric materials: Progress and challenges. *J. Magnes. Alloys* **2022**, *10*, 1719–1736. [[CrossRef](#)]
59. Xinfeng, S.; Chem, P.; Phys, C. Low effective mass and carrier concentration optimization for high performance p-type Mg<sub>2</sub>(1-x)Li<sub>2x</sub>Si<sub>0.3</sub>Sn<sub>0.7</sub> solid solutions. *Phys. Chem. Chem. Phys.* **2014**, *16*, 23576–23583.
60. Huang, L.; Liu, T.; Mo, X.; Yuan, G.; Wang, R.; Liu, H.; Lei, X.; Zhang, Q.; Ren, Z. Thermoelectric performance improvement of p-type Mg<sub>3</sub>Sb<sub>2</sub>-based materials by Zn and Ag co-doping. *Mater. Today Phys.* **2021**, *21*, 100564. [[CrossRef](#)]
61. Huang, Y.; Zheng, S.; Liao, H.; Qiao, S.; Han, G.; Wang, G.; Huang, Z.; Li, J.; Lu, X.; Zhou, X. Synergistic modulation of the thermoelectric performance of melt-spun p-type Mg<sub>2</sub>Sn via Na<sub>2</sub>S and Si alloying. *J. Mater. Chem. A* **2022**, *10*, 5452–5459. [[CrossRef](#)]
62. Xu, F.; Li, A.; Rao, Y.; Huang, Z.; Wei, S. Effect of Aluminum Doping on Microstructures and Thermoelectric Properties of BiCuSeO Thermoelectric Materials. *Trans. Indian Inst. Met.* **2021**, *74*, 2367–2377. [[CrossRef](#)]
63. Yang, T.; Huang, L.; Guo, J.; Zhang, Y.; Feng, J.; Ge, Z. Enhanced Thermoelectric and Mechanical Properties of BaO-Doped BiCuSeO δ Ceramics. *Appl. Energy Mater.* **2021**, *4*, 13077–13084. [[CrossRef](#)]

64. Liu, Y.; Lan, J.; Xu, W.; Liu, Y.; Pei, Y.L.; Cheng, B.; Liu, D.B.; Lin, Y.H.; Zhao, L.D. Enhanced thermoelectric performance of a BiCuSeO system via band gap tuning. *Chem. Commun.* **2013**, *2*, 8075–8077. [[CrossRef](#)] [[PubMed](#)]
65. Liu, Z.; Guo, X.; Li, R.; Qin, J.; Li, H.; Chen, X.; Zhou, X. Band structure manipulated by high pressure-assisted Te doping realizing improvement in thermoelectric performance of BiCuSeO system. *J. Mater.* **2019**, *5*, 649–656. [[CrossRef](#)]

**Disclaimer/Publisher’s Note:** The statements, opinions and data contained in all publications are solely those of the individual author(s) and contributor(s) and not of MDPI and/or the editor(s). MDPI and/or the editor(s) disclaim responsibility for any injury to people or property resulting from any ideas, methods, instructions or products referred to in the content.